13

# Study of the dynamics of heating anode units in a maskless nanolithograph based on an array of microfocus X-ray tubes

© P.Yu. Glagolev, G.D. Demin, N.A. Djuzhev, M.A. Makhiboroda, N.A. Filippov

National Research University of Electronic Technology,
124498 Zelenograd, Moscow, Russia
e-mail: skirdovf@mail.ru

*Received April 30, 2021*
*Revised April 30, 2021*
*Accepted April 30, 2021*

In this paper, we study the dynamics of heating the matrix of anode nodes membrane with a transmission-type target under the action of a field emission current generated in the electronic system of a maskless X-ray nanolithograph. The promising membrane materials that provide the most efficient heat removal from the matrix have been determined, among which diamond-like films have shown the best thermal stability. At the calculated power of soft X-ray radiation $P_X = 2.5$ nW, scattered by a pixel with a size of 20 nm and an X-ray resist irradiation dose $D = 100$ J/m$^2$, the exposure time was 25 $\mu$s. It is shown that during the exposure of a 150 mm plate, a diamond-like anode membrane with a size of 300 × 300 elements heats up from 20 to 62°C, which is 15-25 times lower than the heating temperature of alternative anode materials (Cu, Fe, Ni, Si, Al). The technological route for the fabrication of the matrix of anode nodes is described, taking into account the proposed methods for optimizing its design, aimed at reducing the thermal effects of heating during X-ray nanolithography processes. The results obtained can be applied in the development of a thermostable system of microfocus X-ray tubes as part of a maskless X-ray nanolithograph.

**Keywords:** X-ray nanolithography, microfocus X-ray tube, transmission-type target, matrix of anode nodes, electron bombardment heating, thermal expansion, Bosch-process.

DOI: 10.21883/TP.2022.13.52233.132-21

## Introduction

Over the last ten years the rapid revival of vacuum nanoelectronics, mainly related to process capabilities appearing for implementation of the new types of vacuum devices with conducting channel length of at least 100 nm is observed [1–3]. One of the priority areas of vacuum nanoelectronics is a field-emission electronics, where on the back of the large amount of fundamental and breakthrough studies in this area [4–7], it has been possible to achieve significant practical results and implement the high-technology electronic devices with the field-emission operating principle (diodes [8,9], nanotransistors [10,11], nanosensors [12], portable X-ray tubes [13], etc.). Therefore, the possibility of manufacturing the maskless nanolithograph, based on array of microfocus X-ray tubes, is of the great interest for industrial manufacturing.

Thus far, two basic types of maskless methods of lithography are distinguished for industrial application — optical and electron lithography [14,15]. Disadvantage of optical maskless lithography is a low resolution, that allows to provide the layout forming with technology node of more than 200 nm [16,17]. It is obvious that the most universally-applied and advanced method is the electron lithography. It meets almost all the requirements to hypothetic maskless lithograph, except for one — productive capacity, which drops by six-seven orders with topology decrease from micrometric to nanometric level [14]. The highest expectations are related to multi-beam electron lithography. Due to small wavelength of event the slowest electrons this technology potentially provides the fundamental limitation of resolution on a level of 1 nm. The main problem of electron lithography is an electro-magnetostatic interaction between the nanobeams, resulting in image blurring. Despite the fact that the multi-beam electron lithography is known for decades, this problem is not solved yet. Particularly, the best results have been achieved by Mapper Technology. The last generation unit works with 65 thous. of beams and supports the design rules of 32 nm. Elementary beam size is 25 nm, production capacity is up to 4 plates per hour. These studies have observed the problem of the plates excessive heating and, as a result, limitations of resolution and registration accuracy.

Therefore, the studies in the area of the maskless X-ray lithography are very important for the development of the next generation nanoelectronics. This is applicable both to classical high-production lithography in terms of wavelength selection shorter than 13.5 nm and technologies of multi-layer mirrors manufacturing with diffraction quality, and to creation of key technologies of the maskless X-ray lithography.

In the previous studies [18–20] we proposed the concept of X-ray nanolithograph based on array of microfocus X-ray tubes (MXT). Technologically, such MXT array consists of matrix of anode nodes with transmission-type target, as well as field-emission cathode nodes matrix and control

(grid) electrode holes matrix, self-aligned between each other and creating the matrix of the field-emission cathode-grid nodes (FECN) (Fig. 1). The basis of the single FECN is semiconducting needle-type cathode, intended for generation of the field-emission current under exposure of extraction voltage of the anode and control voltage of the grid electrode, locking or unlocking the corresponding channel for electrons emission. The single anode node consists of beryllium transmission-type target and section of anode membrane (anode electrode) with X-ray window (hole in anode node, defining the direction of X-ray radiation at the exit from the transmission-type target). The transmission-type target is intended for energy conversion of electrons, coming from FECN, „open“ for current flowing, to soft X-ray radiation. Anode electrode with the X-ray window performs two main functions — self-alignment with the transmission-type target and electrical field generation between FECN and the transmission-type target as a result of the extraction voltage application to it. It should be noted that FECN matrix and matrix of anode nodes are self-aligned and have dimension of $300 \times 300$ elements with a step of $3\mu$m.

For the purpose of assurance of reliability and reproducibility of X-ray nanolithography processes the special attention should be made to the stable operation of individual MXT elements and the whole system in general. In the previous study [21] we discussed the methods and ways of improvement of electrostatic stability of matrix of anode nodes. However, the equally important factor, that affects the operation of the whole X-ray system, is its resistance to temperature impacts, since bombardment of the transmission-type target with high-energy electrons (with energy of up to 2 keV and more) can result in significant heating of matrix of anode nodes. It results in significant thermal deformation of matrix of anode nodes, that can negatively affect the operation of the whole device [22]. In its turn, the thermal expansion of matrix of anode nodes material can result in reduction of X-ray window diameter in the corresponding single anode node and, as a result, in reduction of X-ray radiation output power in this area. Thus, it can result in increase of the corresponding X-ray radiation dose refill time for the sensitive X-ray resist exposure. Also, the direction of X-ray radiation at the exit from the individual anode node is defined by the spatial position of the walls of the corresponding X-ray window. During thermal deformation of matrix of anode nodes the deflection of anode membrane is possible, resulting in deviation from the vertical position of the X-ray windows walls. As a result, the direction of X-ray radiation at the exit from the matrix of anode nodes changes, that can result in distortion and blurring of the layout on a plate. Also, the anode heating to temperature above critical value (more than 1400°C for Si) can result in irreversible consequences — degradation and melting of the whole structure or individual elements of the matrix of anode nodes.

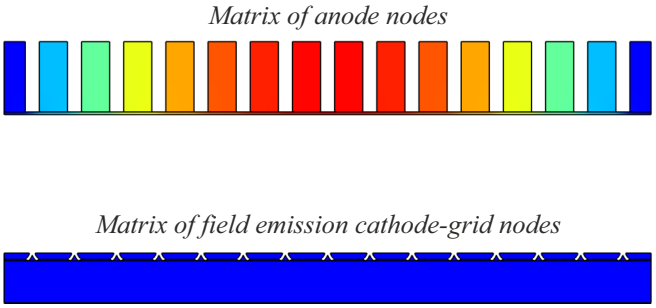


**Figure 1.** Schematic image of soft X-ray radiation source system based on FECN matrix and matrix of anode nodes. FECN matrix consists of silicon needle-type cathode with control grid electrodes. Matrix of anode nodes of initial structure consists of beryllium transmission-type target located on a perforated electrode of anode. Color scheme is presented for displaying of matrix of anode nodes heating at exposure of emission current from FECN matrix.

To prevent from such undesirable effects it is necessary to examine the possible mechanisms of heat removal from the matrix of anode nodes. Heat removal in X-ray tubes is very often performed by means of active air or liquid cooling system, contacting with the heated anode [23]. However, in case of X-ray nanolithograph, such active cooling system requires increasing complexity of the X-ray optical system design. Therefore, the most preferable is the passive cooling of the matrix of anode nodes by means of selecting the optimum composition of materials of the transmission-type target and anode membrane, which allow to provide the high-efficient heat removal from the matrix to the remaining structure of the nanolithograph. For that purpose it is interesting to examine various types of materials with high thermal conductivity $k$, from which we selected the following in our study: C ($k = 2500\,\mathrm{W \cdot m^{-1} \cdot K^{-1}}$), Al ($k = 237\,\mathrm{W \cdot m^{-1} \cdot K^{-1}}$), Cu ($k = 401\,\mathrm{W \cdot m^{-1} \cdot K^{-1}}$), Si ($k = 130\,\mathrm{W \cdot m^{-1} \cdot K^{-1}}$), Ni ($k = 90.7\,\mathrm{W \cdot m^{-1} \cdot K^{-1}}$) and Fe ($k = 80.2\,\mathrm{W \cdot m^{-1} \cdot K^{-1}}$).

## 1. Description of matrix of anode nodes heating model

To calculate the heating of matrix of anode nodes under impact of the directional electron beams from FECN matrix in COMSOL MultiPhysics software environment the evaluation of the beam spot area $S_D$ on anode membrane at the specified distance $d_{CA} = 10\,\mu$m between the tips of the needle-type cathode and anode (at voltage on anode of $V_A = 2\,\mathrm{kV}$ and voltage of $V_G = 30\,\mathrm{V}$ on a grid electrode) was performed on the first stage. This calculation was performed by means of building the electron path from the cathode surface at the specified electric field distribution $\mathbf{E}(\mathbf{r}) = -\nabla\varphi(\mathbf{r})$ in interelectrode space, that corresponds to

equations:

$$\frac{dm_e\mathbf{v}(\mathbf{r})}{dt} = q_e\,\mathbf{E}(\mathbf{r}), \quad (1)$$

$$\nabla^2\varphi(\mathbf{r}) = -\rho_v\varepsilon_0, \quad (2)$$

where $m_e$, $q_e$ are electron mass and charge, $\mathbf{v}(\mathbf{r})$ is electrons velocity, $\varphi(\mathbf{r})$ is potential distribution in interelectrode space, $\varepsilon_0$ is dielectric constant, $\rho_v$ is charge density. The simulation results showed that the beam spot radius on the target is $R \approx 350$ nm. Electrons density distribution over the beam spot is not evenly and can be described with Gaussian function (corresponds to normal distribution). Since within the circle, limiting 50% of the beam spot area, are almost 90% of electrons, the effective radius $R_{\text{eff}} = R/\sqrt{2}$ is introduced, while the effective area of the beam spot is evaluated as $S_D = \pi R_{\text{eff}}^2 \approx 0.196\,\mu\text{m}^2$. Considering electron beam power $P_e$, coming to a single anode node, and total area $S_D^{\Sigma} = \sum_{i=1\ldots n}$ of membrane sections, affected by current through $n$ channels open for emission, the total dissipation power of electron beams $Q_s = P_e^{\Sigma}/S_D^{\Sigma}$, participating in matrix of anode nodes structure heating, was defined, where $P_e^{\Sigma} = \sum_{i=1\ldots n} P_e^i$. Then the numerical calculation of heating temperature of the anode membrane with the specified structure, materials and layers composition was performed, for which the heat conduction equation was used, generally written as:

$$\rho C_p\left(\frac{\partial T}{\partial t} + \mathbf{u}_{\text{trans}}\nabla T\right) + \nabla(\mathbf{q} + \mathbf{q_r}) = Q_S, \quad (3)$$

where $\rho$ is density [kg/m$^3$]; $C_p$ is specific thermal capacity at constant pressure [J/(kg · K)]; $T$ is absolute temperature [K]; $\mathbf{u}_{\text{trans}}$ is heat transfer velocity vector [m/s]; $\mathbf{q} = -k\nabla T$ is convective heat flux vector [W/m$^2$], $k$ is thermal conductivity [W/m · K]; $\mathbf{q_r}$ is heat flux vector from radiation [W/m$^2$].

Calculation of time of exposure of individual X-ray resist section allows to evaluate operating speed of the developed nanolithograph and time of exposure of the whole plate. It should be noted that preliminary evaluation of the time of exposure of individual X-ray resist section is required for simulation of matrix of anode nodes heating under emission current impact with FECN matrix within this time. Time of exposure $t_{\text{exp}}$ of individual section (pixel) of X-ray resist can be evaluated as:

$$t_{\text{exp}} = D/P_S, \quad (4)$$

where $D$ is sensitive X-ray resist radiation dose and $P_S$ is X-ray radiation dissipation power on a pixel, that can be calculated with known X-ray radiation power $P_X$ and single pixel area $S_{pix}$:

$$P_S = P_X/S_{pix}. \quad (5)$$

Calculation of X-ray radiation power $P_X$, coming to X-ray resist, was performed using the equation from [24]:

$$P_X = P_e C_E R_m^2 \Omega_{in}/4\pi. \quad (6)$$

where $C_E$ is coefficient of electrons power $P_e$ conversion to X-ray radiation line power, $R_m$ is reflection coefficient of two-mirror lens X-ray Mo/Be mirrors, examined in [25], $\Omega_{in}$ is solid angle, within which the source radiation falls onto the lens (source useful radiation).

## 2. Evaluation of X-ray resist exposure time

Using the equations (4)–(6) the time of exposure $t_{\text{exp}}$ of individual section of X-ray resist was evaluated. Conversion coefficient for beryllium film with thickness of 200 nm and electrons energy of 2 kV is $C_E = 2.5 \cdot 10^{-4}$ [24], electrons power — $P_e = 2 \cdot 10^{-5}$ W, solid angle $\Omega_{in} = 2\pi$, reflection coefficient of multi-layer X-ray Mo/Be mirrors in spectral range of X-ray radiation (near 11.4 nm) $R_m = 0.7$ [26]. Electron beam power from a single anode node can be calculated with known emission current from a single needle-type cathode $I_{single} = 10$ nA and voltage between anode electrode and FECN matrix $V_{CA} = 2$ kV using formula $P_e = I_{single}V_{CA}$. By substituting all the variables into equation (6) it is possible to calculate X-ray radiation power, equal to $P_X = 1.25 \cdot 10^{-9}$ W. As per [27], pixel diameter of the developed lithograph is 20 nm, therefore the dissipation power of X-ray radiation on pixel, according to equation (5), will be equal to

$$P_S = 1.25 \cdot 10^{-9} \Big/ \left(\pi(10^{-8})^2\right) \approx 0.4 \cdot 10^7\ \text{W/m}^2.$$

Since radiation dose for the sensitive X-ray resist is $D = 10^2$ J/m$^2$ [27], the exposure time is $t_{\text{exp}} = 25\,\mu$s. It should be noted that the developed microfocus lithograph is designed for matrix of $300 \times 300$ elements, therefore it is capable to simultaneously reveal the X-ray resist section with an area of $36\,\mu\text{m}^2$.

## 3. Technological steps for fabrication of the matrix of anode nodes with transmission-type target

In case of silicon (Si) selection as anode material during matrix of anode nodes fabrication the Bosch-process of Si etching to a depth, equal to anode electrode thickness, is performed using Al mask (Fig. 2, *a*). Then Al is etched and oxidation is performed to 100 nm (to prevent from alkaline etchant entering the channels and etching the silicon). If it is necessary to make anode electrode of diamond-like film ($C$), it is deposited in silicon substrate. Then, using reactive ion etching, the channels are etched for X-ray windows over the whole thickness of anode electrode. It should be noted that the lower limit of anode electrode thickness is $5\,\mu$m, since thinner anode electrode will be subject to strong electrostatic deformation [21]. At the same time if the selected diameter of the X-ray windows is 500 nm, the upper limit of anode thickness is $10\,\mu$m, since for the

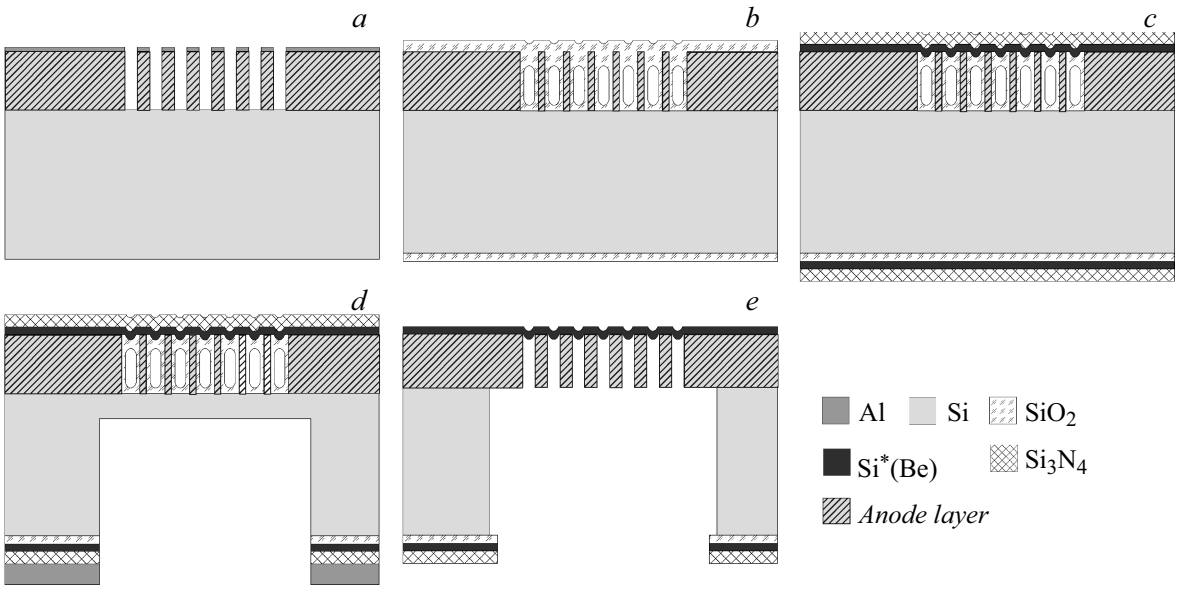


**Figure 2.** Technological steps for fabrication of the matrix of anode nodes with transmission-type target: *a* — Bosch-process using Al mask (reactive ion etching); *b* — melting of borophosphosilicate glass (BPSG); *c* — deposition of $Si_3N_4$; *d* — Bosch-process from the plate back side; *e* — etching of BPSG and $SiO_2$ from channels in HF vapors.

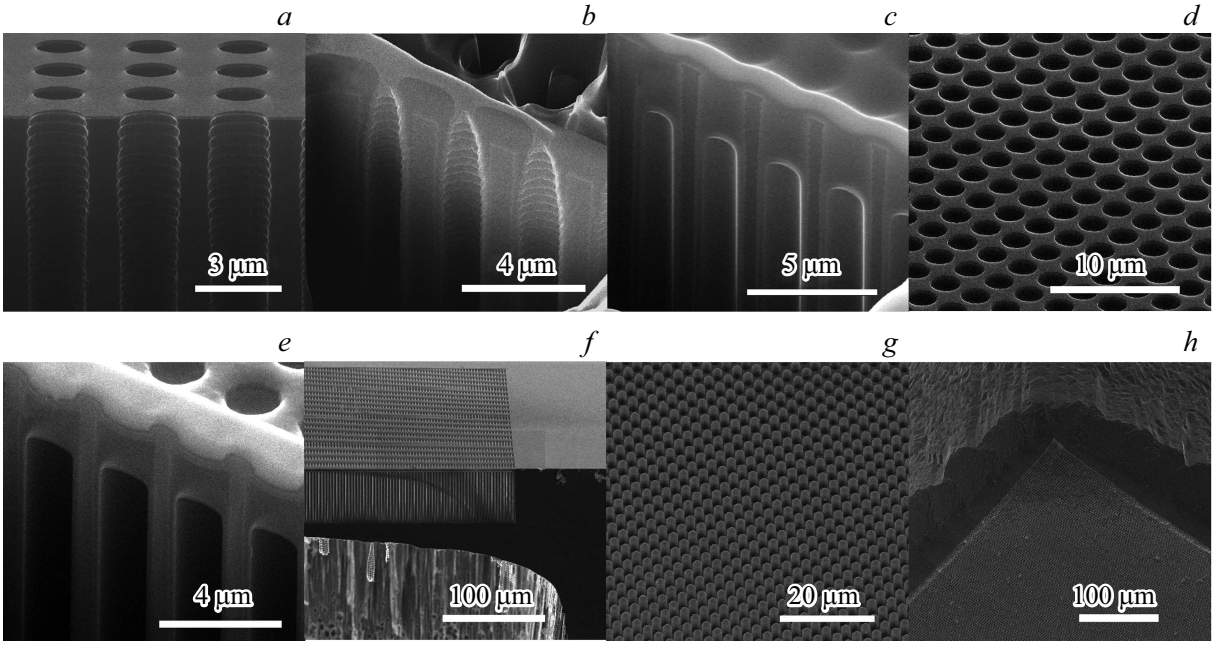


**Figure 3.** Pictures of matrix of anode nodes with the transmission-type target at various route operations, observed using a scanning electron microscope: *a* — Bosch-process of channels etching; *b* — plasma-enhanced chemical vapor deposition (PE CVD) of BPSG; *c* — BPSG melting; *d* — plasma-chemical etching of BPSG; *e* — deposition of $Si^*$ and $Si_3N_4$; *f* — Bosch-process of etching from the membrane back side; *g* — final etching of silicon from the back side in 40% solution of KOH; *h* — removal of BPSG and $SiO_2$ in concentrated HF vapors with $C_2H_5OH$.

specified size of channels the reactive ion etching does not allow to reach higher aspect ratios ($> 20$).

Then, regardless of anode electrode material selection, the deposition of $2\,\mu$m of borophosphosilicate glass (BPSG) is performed and its melting in atmosphere of $N_2$. After deposition BPSG does not form a continuous layer, having ruptures in film above holes. During melting due to surface tension the BPSG closing is happened above the holes and continuous layer is formed. At the same time the base volume of BPSG remains near surface, plugging the hole above (Fig. 2, *b*). Then the plasma-chemical etching of BPSG is performed until it is removed from the surface.

After that the deposition of the target layer of Be or Si* is performed. Selection of target material is mainly related with the necessity of observing the characteristic radiation with a wavelength near 11.4 nm, to which the X-ray optical system is set. Therefore, the process operations of thin Be and Si* films forming, meeting the specified requirement, is developed. Then, the deposition of $Si_3N_4$ layer is performed (Fig. 2, *c*). At the next stage the sputtering of Al on the back side and photolithography with the following alignment to the front side are performed. Then, on the back side the layers are etched and Bosch-process of silicon etching is performed. Etching time should not allow the silicon substrate to be etched down to channels (Fig. 2, *d*). The following process operation is aluminum mask etching from the back side. Final etching of silicon is performed in alkali solution (to lower the defects from Bosch-process and to improve controllability). After that the nitride etching on the front side is performed. Then, $SiO_2$ and BPSG are etched from the channels in HF vapors and using plasma-chemical etching. As a result of the performed process operations the thin membranes, having electrical contact with a substrate and hanging over the channels, are manufactured (Fig. 2, *e*). Fig. 3 shows the images of a structure of matrix of anode nodes with transmission-type target at individual process stages of manufacturing, observed, as per the selected process flow, using scanning electron microscope.

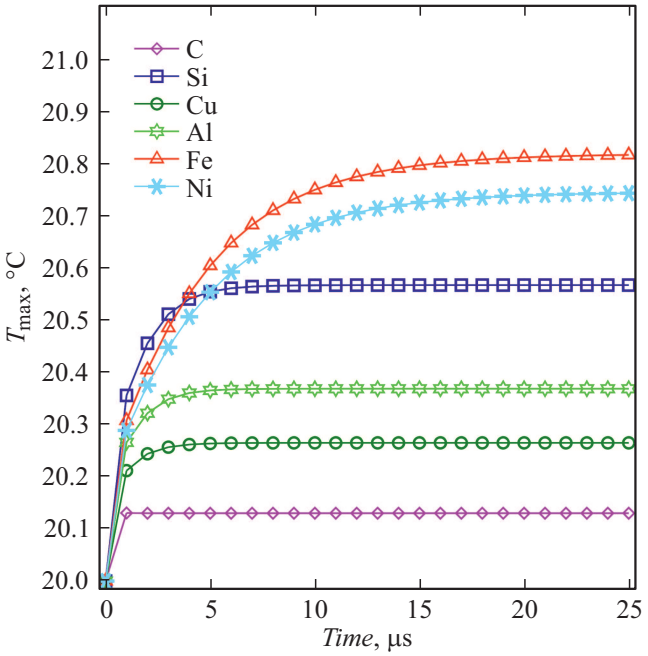


**Figure 4.** Dependence of maximum temperature of matrix of anode nodes on a time of heating with emission current from FECN matrix for various materials of anode electrode (C, Si, Cu, Al, Fe, Ni).

## 4. Simulation results

As was already mentioned, the matrix of anode nodes is a beryllium transmission-type target and anode electrode with X-ray windows $300 \times 300$ matrix. Matrix of anode nodes is made as a round membrane with radius of $750\,\mu$m. To understand the general dependencies the model was simplified (number of cells in X-ray windows matrix was reduced). Material type and anode electrode thickness influence on maximum temperature of matrix of anode nodes heating was evaluated. Also the dependence of maximum temperature on the transmission-type target thickness is presented. These evaluations are presented for both short interval (X-ray resist exposure time) and the whole plate exposure operation (several hours).

Physico-mathematical simulation was performed in COMSOL Multiphysics software package [28]. The „Heat Transfer in Solids“module, that describes heat transfer in solids using heat conduction law and heat balance equations, was selected for simulation. The „Boundary Heat Source“boundary condition, that is a member of equation (3) $Q_b = P_e/S_{beam}$, responsible for additional heat sources, was used for description of Joule heating of matrix of anode nodes with the field-emission current from FECN matrix. It should be noted that $P_e$ is electron beam power from individual cathode, $S_{beam}$ is characteristic area of electron beam, coming to the transmission-type target. X-ray lithograph is a more massive structure, than matrix of anode nodes, therefore it can conditionally be assumed that the whole remaining structure of X-ray lithograph has the constant temperature. Therefore, another boundary condition is defined - „Temperature“, that sets the constant temperature (20°C) at side edges of matrix of anode nodes, that contact with the remaining structure of the lithograph. Since external boundaries of matrix of anode nodes contact with vacuum during its heating with current from FECN matrix, convection and heat dissipation into environment may be neglected. Therefore, the calculations assume that the heat flux at external boundaries of the matrix is equal to zero.

The important aspect of matrix of anode nodes structure is a selection of anode electrode material (> 95% of matrix of anode nodes volume), since matrix of anode nodes should have high strength, electrostatic stability, high thermal conductivity and thermal capacity for fast heat removal and prevention of this node overheating. In the article [21] the methods and recommendations for improving the strength and electrostatic stability of matrix of anode nodes are described, therefore in this study we will examine the methods of reduction of heating of matrix of anode nodes in detail. Fig. 4 shows the dependence of maximum temperature of matrix of anode nodes on a time of emission current impact on the transmission-type target for materials (C — diamond-like films, Si, Cu, Al, Fe, Ni), often used in microelectronics. For calculations simplification the matrix of anode nodes with a size of $10 \times 10$ elements was demonstrated, while anode electrode thickness was $5\,\mu$m, transmission-type target thickness —

200 nm, matrix of anode nodes radius — 25 $\mu$m. Fig. 4 shows that within the sensitive X-ray resist exposure time (25 $\mu$s) the maximum heating of matrix of anode nodes does not exceed 1°C for any of the mentioned materials. Anode nodes matrices with anode electrode of C, Cu and Al were subject to lower heating, since they have higher thermal conductivity, than other materials. Another feature of this graph is that for anode electrode of C, Cu, Si and Al the maximum temperature of matrix of anode nodes quickly (within several $\mu$s) reaches plateau, while for Ni and Fe the maximum temperature continues to rise within the whole time.

After selection of matrix of anode nodes material the most obvious method for matrix of anode nodes heating reduction is the determination of optimum thickness of anode electrode. Reduction of anode electrode thickness can result in electrostatic deformation and later to stickiness of the matrix of anode nodes and a grid (of control electrode), that was described in article [21]. Fig. 5 shows the dependence of maximum temperature of matrix of anode nodes under exposure of emission current from FECN matrix to the transmission-type target within 10 $\mu$s on anode electrode thickness. Geometrical dimensions of matrix of anode nodes parameters were the same as described above. Dependencies in Fig. 5 show that increase of anode electrode thickness results in reduction of the maximum temperature of matrix of anode nodes heating for all materials under study (C, Si, Cu, Al, Fe, Ni). It should be noted that the diamond-like films demonstrate the best heat removal compared to other materials, since the maximum temperature of matrix of anode nodes heating

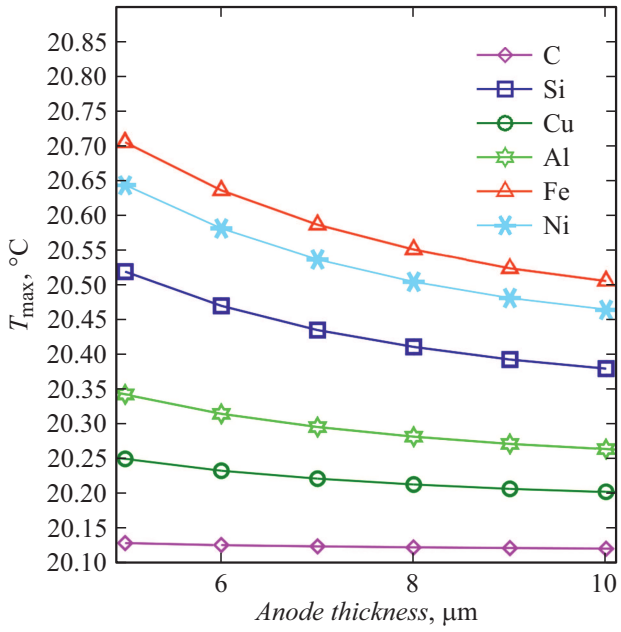


**Figure 5.** Dependence of maximum temperature of matrix of anode nodes on anode electrode thickness due to heating with emission current from FECN matrix within 10 $\mu$s for various materials of anode electrode (C, Si, Cu, Al, Fe, Ni).

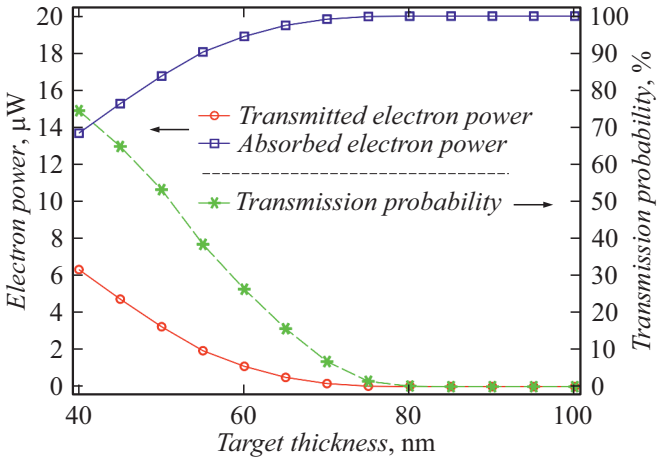


**Figure 6.** Dependence of power, absorbed by the transmission-type target, and percentage of electrons, passed through the target, on thickness of the beryllium transmission-type target.

was almost the same. Since the optimum cone angle (wall inclination) of X-ray windows should be equal to 2.5° due to the requirements to projection lens (numerical aperture NA = 0.4, 10× increase) for the specified size of X-ray windows (R = 250 nm) and matrix step (distance between windows is 3 $\mu$m), the anode electrode thickness can not exceed 25 $\mu$m. This is because at higher values of anode thickness the closing of X-ray windows happens, or their dividing wall becomes extremely thin (distance between windows boundaries is less than 300 nm).

From study [24] it follows that the conversion coefficient significantly varies with thickness of beryllium transmission-type target. In this study it is also shown, that the maximum of the conversion coefficient of electrons energy of 2 keV is achieved with target thickness of 40 nm. However, beside the conversion coefficient, during operation of X-ray nanolithograph the equally important parameter is the maximum temperature of matrix of anode nodes heating. Matrix of anode nodes is heated by means of Joule heat from the transmission-type target, that is generated at the exposure of the field-emission current from FECN matrix to the target. The performed calculations show that the region of maximum temperature of matrix of anode nodes heating is directly on the bottom edge of the transmission-type target (in its center).

The calculation was performed, based on results of which the dependence of the percentage of passed electrons on the transmission-type target thickness for thin (< 100 nm) beryllium films was observed (Fig. 6). According to our calculations, share of passed electrons for a target with thickness of 40 nm is about 75%. It should be noted that electrons, going out of the target, during passing through the target still give part of their kinetic energy to lattice atoms. To define the energy, absorbed by the transmission-type target, the kinetic energy of each passed electron should be known. The formula for calculation of power, absorbed

by the transmission-type target, is proposed:

$$P_{abs} = P_e - \sum_{i=1}^{n} \varepsilon_i / t_i, \qquad (7)$$

where $\varepsilon_i$ is energy of the $i$-th electron, passed through the target, $t_i$ is time of the $i$-th electron passing through the transmission-type target. According to this formula, the dependence of power, absorbed by the transmission-type target, on thickness of the beryllium transmission-type target is built (Fig. 6). Despite the high share of electrons (near 75%), passed through the transmission-type target ($h = 40$ nm), in average they lost about 59% energy at collisions in the target atoms. Therefore, the share of the absorbed energy is about 69% from initial (before hitting the target) or 13.8 $\mu$W from each FECN. This value will be used at calculations of the maximum temperature of anode node heating. At reaching the transmission-type target thickness of more than 80 nm all electrons are absorbed by the transmission-type target.

Then, the simulation was performed, based on results of which the dependence of the maximum temperature of matrix of anode nodes heating on the beryllium transmission-type target thickness was built considering power, absorbed by the target, for anode electrode of C and Si (see Fig. 7). Simulation was performed for matrix of anode nodes with a size of $10 \times 10$ elements, anode electrode thickness was 5 $\mu$m, matrix of anode nodes radius — 25 $\mu$m, heating with emission current was performed within 25 $\mu$s. Fig. 8 shows the distribution of the temperature of the matrix of anode nodes from the transmission-type target thickness due to heating with the emission current from FECN matrix. As shown in Fig. 7, for matrix of anode nodes, anode

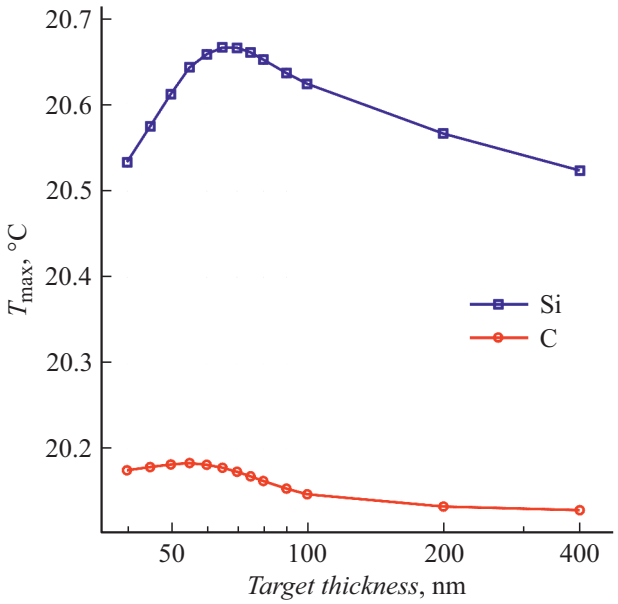


**Figure 7.** Dependence of the maximum temperature of the matrix of anode nodes on the transmission-type target thickness due to heating with the emission current from FECN matrix within 25 $\mu$s.

electrode material of which is silicon, the maximum heating temperature is achieved at the transmission-type target thickness of 65 nm. This effect can be explained by the fact, that at the beryllium transmission-type target thickness of less than 70 nm the sharp drop of the power, absorbed by the target, starts (Fig. 7). At the same time, for matrix of anode nodes, anode electrode material of which is diamond-like film, the maximum heating temperature is achieved at the transmission-type target thickness of 55 nm. As opposed to matrix of anode nodes with Si anode electrode, the temperature extremum for matrix of anode nodes with C anode electrode is observed at lower thickness of the transmission-type target due to high thermal conductivity of C ($k = 2500\,\mathrm{W \cdot m^{-1} \cdot K^{-1}}$). It should be noted that the ratio of area of side surface (proportional to the product of thickness by diameter) of the transmission-type target and area of contact between the transmission-type target and anode electrode plays an important role in matrix of anode nodes heating.

X-ray windows matrix on the top view is a square with $Nk$ side, where $N$ is matrix dimension, $k = 3\,\mu$m is matrix step. At the same time, the matrix of anode nodes is a round membrane with radius $R$. There is some gap from the edge of X-ray windows matrix to the membrane edge, equal to $W_{edge} = R - (Nk/2)$. Dependence of the maximum temperature of matrix of anode nodes during exposure of the emission current from FECN matrix on the value of gap $W_{edge}$ was demonstrated for $10 \times 10$ matrix (Fig. 9). Thickness of anode electrode and the transmission-type matrix was 5 $\mu$m and 200 nm, respectively, heating with the emission current was performed within 10 $\mu$s. Anode electrode of C, Si, Cu and Al demonstrated growth of the maximum temperature of the matrix of anode nodes heating with increase of the value of gap $W_{edge}$, while for Ni and Fe there was a growth up to $W_{edge} = 40\,\mu$m, and then — reaching of plateau of the maximum temperature of the matrix of anode nodes heating. This effect is explained by the fact, that the matrix of anode nodes with the anode of Ni and Fe reaches the thermal equilibrium, when $W_{edge} = 40\,\mu$m.

As shown in Fig. 4 and 7, for the majority of the simulated materials of the anode electrode the maximum temperature of matrix of anode nodes heating reaches the „plateau“ (maximum) within a short time period ($< 10\,\mu$s). This effect can be explained by the fact, that the boundary condition of the constant temperature for the membrane side edges constrains the further growth of the matrix of anode nodes temperature, since the membrane radius for X-ray windows matrix of $10 \times 10$ elements is 25 $\mu$m. The actual structure of the matrix of anode nodes assumes the membrane with radius of 750 $\mu$m and thickness of 5–10 $\mu$m. Fig. 10 shows the dependence of the maximum temperature of the matrix of anode nodes heating at exposure with the emission current from FECN matrix on X-ray windows matrix dimensions (number of heating centers). During simulation the following parameters were set: membrane radius is 750 $\mu$m; anode electrode thickness

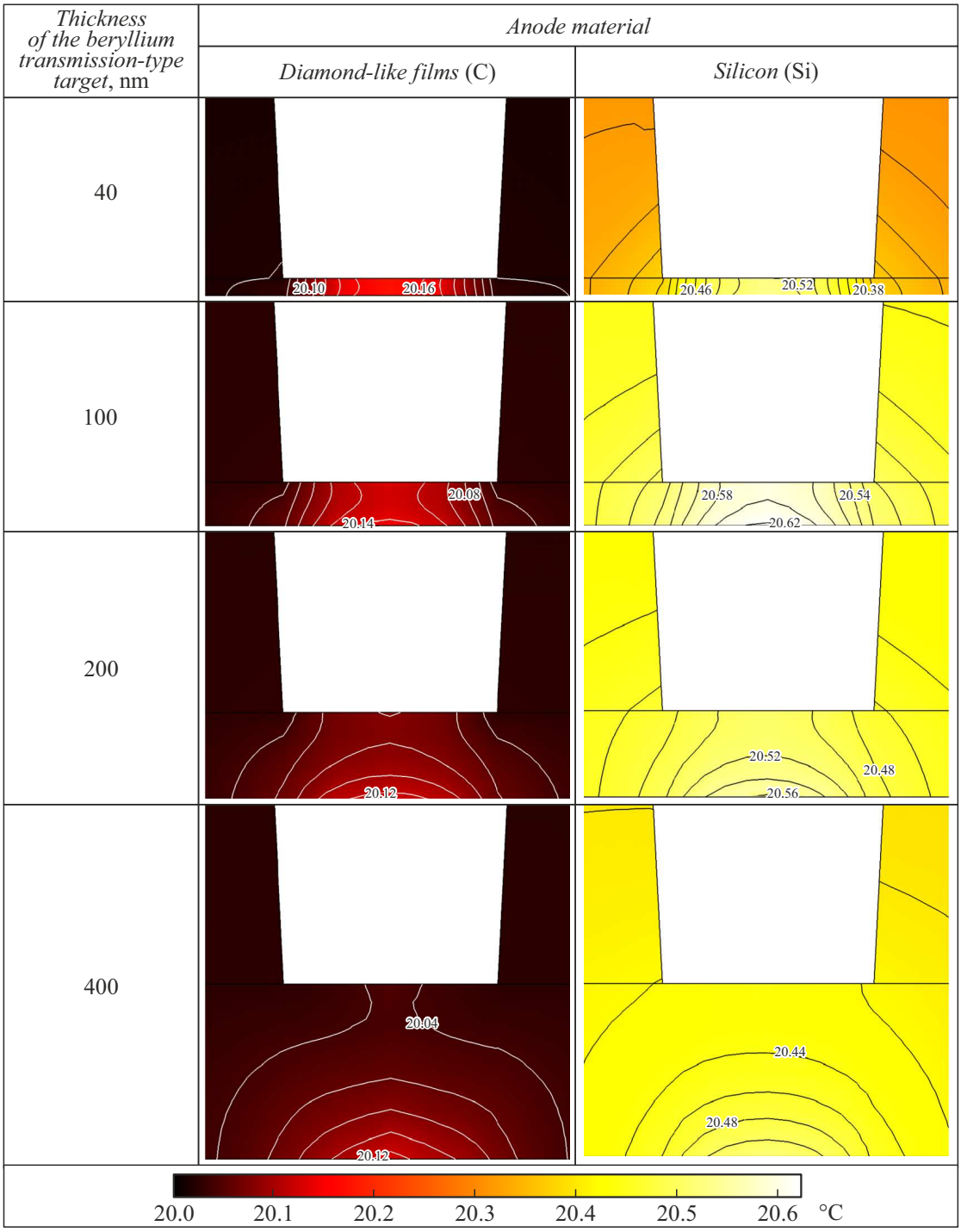


**Figure 8.** Structure cut with thermal distribution, observed as a result of heating with emission current from FECN matrix within 25 $\mu$s, for various thickness of the beryllium transmission-type target (40−400 nm) for anode electrode of C and Si.

is 5 $\mu$m; material of the anode electrode is Si or C; transmission-type target thickness is 200 nm; calculated time of X-ray resist exposure is $10^4$ s (that corresponds with the plate processing time of 150 mm).

Fig. 10 also shows the extrapolating curves, that allow to evaluate the maximum heating temperature for large matrices, up to $300 \times 300$ elements. Extrapolating curves were built based on calculated data for $10 \times 10$, $20 \times 20$, $30 \times 30$, $40 \times 40$ and $50 \times 50$ matrices using MATLAB software package [29]. The following equations were obtained for the extrapolating curves, that can be used for evaluation of the matrix of anode nodes heating: for Si — $y = 0.009399x^2 + 0.1539x + 20$; for C — $y = 0.000408x^2 + 0.01577x + 20$. As shown in Fig. 10,

the maximum temperature of the matrix of anode nodes heating for the anode electrode of Si is $> 900°C$, while for the anode electrode of diamond-like film is $< 65°C$. It

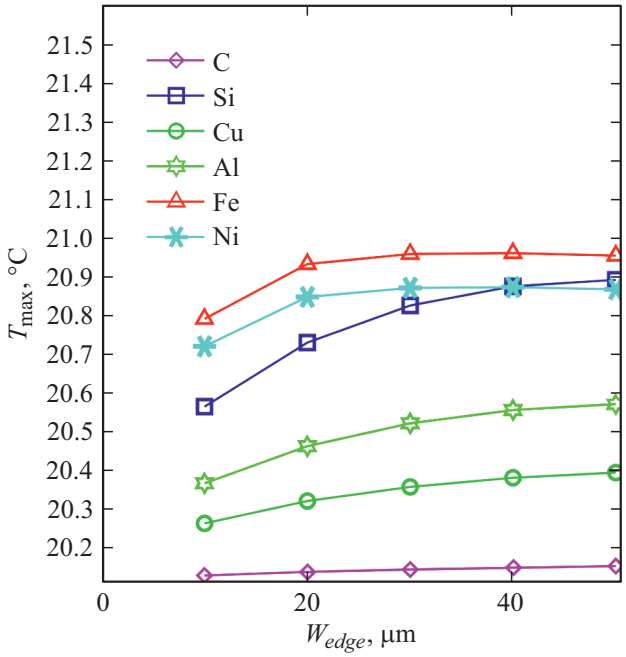


**Figure 9.** Dependence of the maximum temperature of matrix of anode nodes at exposure of the emission current from FECN matrix on the value of gap $W_{edge}$.

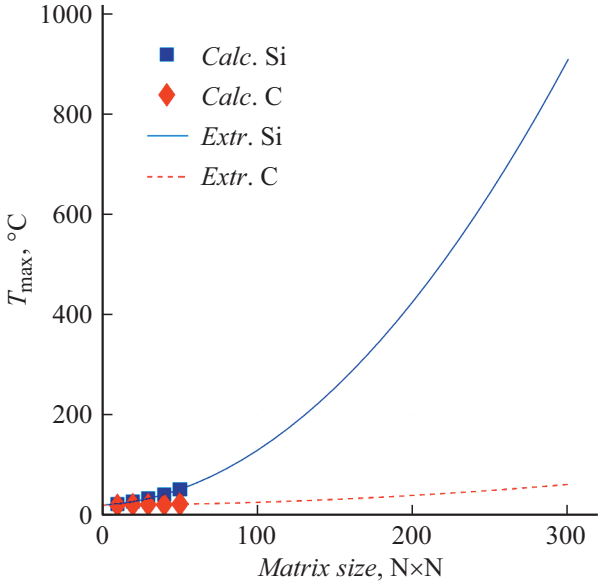


**Figure 10.** Dependence of the maximum temperature of the matrix of anode nodes heating on matrix dimensions. Square markers — calculated values for the matrix of anode nodes with the anode electrode of Si; rhombic markers — calculated values for the matrix of anode nodes with the anode electrode of C; continuous line — extrapolating curve for the anode electrode of Si; dashed line — extrapolating curve for the anode electrode of C. Membrane radius is 750 $\mu$m.

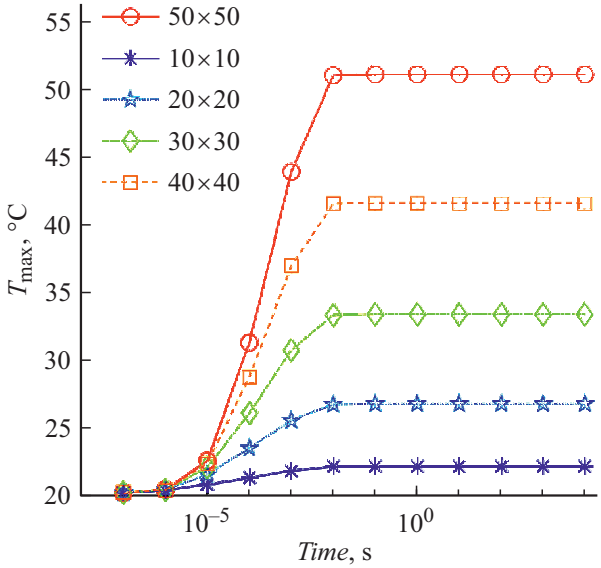


**Figure 11.** Dependence of the maximum temperature of the matrix of anode nodes heating on a time of exposure with emission current from FECN matrix for various matrix dimensions. Anode electrode material is Si. Membrane radius is 750 $\mu$m.

is obvious that the most optimum material for the anode electrode in terms of lowering the anode node heating is C.

Fig. 11 shows the growth dynamics of the maximum temperature of the matrix of anode nodes for various matrix dimensions. The examined model has the following parameters: membrane radius is 750 $\mu$m; anode electrode thickness is 5 $\mu$m; anode electrode material is Si; transmission-type target thickness is 200 nm. Simulation data show that the maximum temperature of the matrix of anode nodes heating reaches the limiting values within a few hundredths of a second.

## Conclusion

Taking all the aforesaid into consideration, it should be said that the important aspect of the correct and accurate operation of X-ray nanolithograph is a temperature stabilization of the complete device and matrix of anode nodes in particular. The reason of failed operation of the X-ray nanolithograph can be the thermal expansion and degradation of the matrix of anode nodes due to its significant heating under exposure of the emission current from FECN matrix to the transmission-type target. One of the methods to lower the matrix of anode nodes heating, examined in this study, is the selection of the matrix of anode nodes material with the highest thermal conductivity and thermal capacity. Based on the developed physico-mathematical model the calculation of the matrix of anode nodes heating was performed for various materials of the anode electrode (anode membrane), among which the most optimum material for the anode electrode in terms of the anode node heating reduction are diamond-like films.

Extrapolation of the calculated dependencies of heating temperature on the matrix dimensions showed that for the matrix of anode nodes of $300 \times 300$ elements the maximum heating temperature for the anode electrode of diamond-like film is not more than $65^\circ$C ($\Delta T = 42$ K).

Methods of the matrix of anode nodes design optimization to reduce its heating and increase heat removal from it were proposed: increase of thickness of the anode electrode and transmission-type target. The calculations showed that increase of the anode electrode thickness by a factor of 2 (from 5 to 10 $\mu$m) results in reduction of the maximum temperature of the matrix of anode nodes heating from 5 to 30% depending on the anode electrode material. Calculations for various thickness (40–400 nm) of the transmission-type target were also performed considering the power, absorbed by the target, for anode electrodes of C and Si; as a result, it was revealed that the extremum of the maximum heating temperature is reached at the transmission-type target thickness of 55 and 65 nm, respectively. This effect is related to the fact, that at the beryllium transmission-type target thickness of less than 70 nm the sharp drop of the power, absorbed by the target, starts (Fig. 7). It should be noted that the increase of the transmission-type target thickness results in reduction of the coefficient of electrons energy conversion to X-ray radiation energy. The optimum range of the transmission-type target thickness in terms of compromise between conversion coefficient and thermal load on the matrix of anode nodes with diamond-like anode electrode is a range of 100–200 nm for electrons energy of 2 keV. Despite the fact that in this range the conversion coefficient reduces by 10–20% in relation to conversion coefficient at selection of the optimum target thickness, equal to 40 nm [24], the maximum temperature of the matrix of anode nodes heating reduces by 20–25%. At the same time, for matrix of anode nodes with silicon anode electrode the most optimum choice in this case is the beryllium transmission-type target with thickness of 40 nm.

Thus, the recommendations, formed during work and focused on reduction of the thermal heating effect of the matrix of anode nodes as part of the soft X-ray radiation sources, may play an important role in improving the stability and reliability of X-ray nanolithography processes based on them. The simulation results can also be applied for development and manufacturing of the small devices for X-ray radiation generation.

### Funding

This work was performed on the equipment of R&D center „MEMSEC“ (MIET) with financial support of the Ministry of Science and Higher Education of the Russian Federation (№ 075-03-2020-216, 0719-2020-0017, FSMR-2020-0017).

### Conflict of interest

The authors declare that they have no conflict of interest.

## References

[1] T. Matsui. J. Infrared Milli Terahz Waves, **38** (9), 1140 (2017). DOI: 10.1007/s10762-017-0387-9
[2] J. Feng, X. Li, J. Hu, J. Cai. J Electromagn. Eng Sci., **20** (1), 1 (2020). DOI: 10.26866/jees.2020.20.1.1
[3] B. Levush. IVEC (Busan, South Korea, 2019), p. 1–5. DOI: 10.1109/IVEC.2019.8745196
[4] S.A. Guerrera, A.I. Akinwande. Nanotech., **27**, 295302 (2016). DOI: 10.1088/0957-4484/27/29/295302
[5] J.-W. Han, M.-L. Seol, D.-I. Moon, G. Hunter, M. Meyyappan. Nat. Electron., **2**, 405 (2019). DOI: 10.1038/s41928-019- 0289-z
[6] M. Liu, T. Li, Y. Wang. J. Vac. Sci. Technol. B, **35**, 031801 (2017). DOI: 10.1116/1.4979049
[7] Y. Huang, Z. Deng, W. Wang, C. Liang, J. She, S. Deng, N. Xu. Sci. Rep., **5**, 10631 (2015). DOI: 10.1038/srep10631
[8] P. Zhang, Y.Y. Lau. J. Plasma Phys., **82**, 595820505 (2016). DOI: 10.1017/S002237781600091X
[9] W.-T. Chang, H.-J. Hsu, P.-H. Pao. Micromachines, **10**, 858 (2019). DOI: 10.3390/mi10120858
[10] J.-W. Han, D.-I. Moon, M. Meyyappan. Nano Lett., **17**, 2146 (2017). DOI: 10.1021/acs.nanolett.6b04363
[11] J. Xu, Z. Gu, W. Yang, Q. Wang, X. Zhang, Nanoscale Res. Lett., **13**, 311 (2018.) DOI: 10.1186/s11671-018-2736-6
[12] M. Liu, Y. Lei, Y. Yang, T. Li, Y. Wang. *Proc. 2019 International Conference on Manipulation, Automation and Robotics at Small Scales* (Helsinki, Finland, 2019), 1. DOI: 10.1109/marss.2019.8860991
[13] N.A. Djuzhev, G.D. Demin, T.A. Gryazneva, V.Yu. Kireev, D.V. Novikov. *Proc. 2018 IEEE Conference of Russian Young Researchers in Electrical and Electronic Engineering* (IEEE, Moscow, Russia, 2018) DOI: 10.1109/EIConRus.2018.8317498
[14] R. Menon, A. Patel, D. Gil, H.I. Smith. Mater. Today, **8** (2), 26 (2005).
[15] G.V. Belokopytov, Yu.V. Ryzhikova. Mikroelektronika, **40** (6), 453 (2011) (in Russian).
[16] U. Dauderstädt, P. Askebjer, P. Björnängen, P. Dürr, M. Friedrichs, M. List, D. Rudloff, J.-U. Schmidt, M. Müller, M. Wagner. Proc. SPIE, **7208**, 720804 (2009).
[17] Electronic source. Available at: https://heidelberg-instruments.com/en/products/dwl-66.html
[18] N.A. Djuzhev, G.D. Demin, N.A. Filippov, I.D. Evsikov, P.Y. Glagolev, M.A. Makhiboroda, N.I. Chkhalo, N.N. Salashchenko, S.V. Filippov, A.G. Kolosko, E.O. Popov, V.A. Bespalov. Tech. Phys., **64** (12), 1742 (2019). DOI: 10.1134/S1063784219120053
[19] N.N. Salashchenko, N.I. Chkhalo, N.A. Djuzhev. J. Surf. Invest.: X-Ray, Synchrotron Neutron Tech., **12**, 944 (2018). DOI: 10.1134/S1027451018050324
[20] G.D. Demin, N.A. Djuzhev, N.A. Filippov, P.Yu. Glagolev, I.D. Evsikov, N.N. Patyukov. J. Vac. Sci. Technol. B, **37**, 022903 (2019). DOI: 10.1116/1.5068688
[21] P.Yu. Glagolev, G.D. Demin, G.I. Oreshkin, N.I. Chkhalo, N.A. Djuzhev. Tech. Phys., **65** (11), 1709 (2020). DOI: 10.1134/S1063784220110122
[22] V.P. Nazmov, E.F. Reznikova, A. Somogyi, J. Mohr, V. Saile. *Optical Science and Technology, the SPIE 49th Annual Meeting* (Denver, Colorado, United States, 2004), p. 235. DOI: 10.1117/12.562615

[23] G.D. Demin, N.A. Dyuzhev, M.A. Makhiboroda, A.Y. Lopatin, N.I. Chkhalo, A.E. Pestov, N.N. Salashchenko. *International Conference on Micro- and Nano-Electronics.* 2018. (Zvenigorod, Russian Federation: SPIE, 2019), p. 67. DOI: 10.1117/12.2522105
[24] A.Ya. Lopatin, D.E. Par'ev, A.E. Pestov, N.N. Salashchenko, N.I. Chkhalo, G.D. Demin, N.A. Dyuzhev, M.A. Makhiboroda, A.A. Kochetkov. J. Exp. Theor. Phys. **127** (6), 985 (2018). DOI: 10.1134/S1063776118100175
[25] N.A. Dyuzhev, G.D. Demin, T.A. Gryazneva, A.E. Pestov, N.N. Salashchenko, N.I. Chkhalo, F.A. Pudonin. Kratk. Soobshch. Fiz. FIAN, **12**, 56 (2017).
[26] C. Montcalm, S. Bajt, P.B. Mirkarimi, E.A. Spiller, F.J. Weber, J.A. Folta. 23rd *Annual International Symposium on Microlithography* (Santa Clara, CA, United States 1998), p. 46. DOI: 10.1117/12.309600
[27] N.A. Dyuzhev, G.D. Demin, T.A. Gryazneva, A.E. Pestov, N.N. Salashchenko, N.I. Chkhalo, F.A. Pudonin. Bull. Lebedev Phys. Inst. **45** (1), 1 (2018). DOI: 10.3103/S1068335618010013
[28] COMSOL Multiphysics, COMSOL AB, Stockholm, Sweden, https://www.comsol.com/
[29] MATLAB, MathWorks, https://www.mathworks.com/products/matlab